

² **Commissioning and performance in beam tests of the**
³ **highly granular SiW-ECAL technological prototype for the**
⁴ **ILC**

⁵ *E-mail:* irles@lal.in2p3.fr

⁶ **ABSTRACT:** High precision physics at future colliders as the International Linear Collider (ILC)
⁷ require unprecedented high precision in the determination of the energy of final state particles. The
⁸ needed precision will be achieved thanks to the Particle Flow algorithms (PF) which require highly
⁹ granular and hermetic calorimeters systems. The Silicon-Tungsten Electromagnetic Calorimeter
¹⁰ (SiW-ECAL) technological prototype design and R&D is tailored to the baseline design of the
¹¹ ECAL of the International Large Detector (ILD) for the ILC. In this document we present the latest
¹² news on R&D of such prototype with fully embedded very front-end (VFE) electronics. Special
¹³ emphasis is given to the presentation and discussion of the commissioning of the prototype for
¹⁴ beam test and to the performance of the device in such beam test carried at DESY in June 2017.

¹⁵ **KEYWORDS:** Calorimeter methods, calorimeters, Si and pad detectors

16	Contents	
17	1 Introduction	1
18	2 The SiW-ECAL engineering prototype	3
19	2.1 Silicon sensors	3
20	2.2 SKIROC: Silicon pin Kalorimeter Integrated ReadOut Chip	4
21	2.3 Active Sensor Units	5
22	2.4 Data AcQuisition system	7
23	2.5 Setup	8
24	3 Commissioning of the detector	8
25	3.1 Optimization of noise levels	9
26	3.2 Threshold determination	10
27	3.3 S/N ratio in the trigger line	12
28	3.4 Prospects	13
29	4 Performance on positron beam test at DESY	14
30	4.1 Pedestal and noise studies with the SiW-ECAL in tracker mode	16
31	4.1.1 Pedestal and noise in large magnetic fields	16
32	4.2 MIP response and tracking efficiency with the SiW-ECAL in tracker mode	18
33	4.2.1 S/N ratio in the ADC	19
34	4.3 Pedestal stability in electromagnetic shower events	20
35	4.4 Fake triggers filtering	21
36	5 Summary and prospects	22

37 **1 Introduction**

38 Future accelerator based particle physics experiments require very precise and detailed reconstruc-
39 tion of the final states produced in the beam collisions. A particular example is the next generation
40 of e^+e^- linear colliders such the ILC[1–5]. This project will provide collisions of polarized beams
41 with centre-of-mass energies (*c.m.e*) of 250 GeV - 1 TeV. These collisions will be studied by two
42 multipurpose detectors: the International Large Detector (ILD) and the Silicon Detector (SiD)[5].
43 Another example of an e^+e^- collider project is the Compact Linear Collider (CLIC) project[6–8]
44 which will produce collisions with *c.m.e* of 380 GeV - 3 TeV with a detector featuring similar
45 design than the ILD and SiD. Both projects will explore with unprecedented precision the origin of
46 the electroweak symmetry breaking and new physics beyond the standard model by exploring final
47 states with heavy bosons (W, Z and H) and fermions (*i.e.* heavy quarks as *c*, *b* and *t*).

48 To meet the required precision levels, these detectors will be based on the Particle Flow (PF)
49 techniques[9–11]. These techniques rely on single particle separation to make possible the choice
50 of the best information available in the full detector to measure the energy of the final state objects:
51 *i.e.* the charged particles momentum is better measured by the tracking system the photons energy
52 by the electromagnetic calorimeter and the neutral hadrons energy by the full calorimeter system.
53 In that way the poor resolution of the calorimeter systems (compared with trackers) will only
54 have a reduced impact in the overall reconstruction. For this purpose, detectors optimized for PF
55 algorithms have some requirements, summarized here:

- 56 • a highly efficient and "transparent" tracking system between the interaction point and the
57 calorimetry systems;
- 58 • highly granular (*imaging calorimetry*) and compact calorimeter systems featuring minimum
59 dead material;
- 60 • and high power of particle separation¹.

61 The R&D of highly granular calorimeters for future linear colliders is conducted within the
62 CALICE collaboration and, for now on, we refer the reader to [11] for further information about PF
63 and the CALICE R&D.

64 In this document we will focus in the description of the silicon-tungsten electromagnetic
65 calorimeter, SiW-ECAL, its commissioning and its performance in beam test. The SiW-ECAL is
66 the baseline choice for the ILD ECAL. It consists in a detector (in the barrel region) of 24 X_0 of
67 thickness which corresponds to $\sim 1 \lambda_I$ (interaction length). It has silicon (Si) as active material and
68 tungsten (W) as absorber material. The combination of Si and W choices makes possible the design
69 and construction of a very compact calorimeter with highly granular and compact active layers.
70 It will consist of an alveolar structure of carbon fiber into which modules called SLABs made of
71 tungsten plates and the active sensors will be inserted. The very-front-end (VFE) electronics will
72 be embedded in the SLABs. The silicon sensors will be segmented in squared cells (or channels)
73 of 5x5 mm: a total of ~ 100 million channels will constitute the ECAL for ILD. The desired
74 signal dynamic range in each channel goes from 0.5 MIP to 3000 MIPs. To reduce overall power
75 consumption, the SiW-ECAL will exploit the special bunch structure foreseen for the ILC: the e^+e^-
76 bunches trains will arrive within acquisition windows of $\sim 1\text{--}2$ ms width separated by ~ 200 ms.
77 During the idle time, the bias currents of the electronics will be shut down. This technique is usually
78 denominated power pulsing. In addition to this, to cope with the large amount of channels, the
79 calorimeters should work in self-trigger mode (each channel featuring an internal trigger decision
80 chain) and zero suppression mode.

81 The first SiW-ECAL prototype was the so called SiW-ECAL physics prototype. It was success-
82 fully tested at DESY, FNAL and CERN running together with another prototype from the CALICE
83 collaboration, the analogue hadronic calorimeter AHCAL, delivering the proof of concept of PF
84 calorimetry. For the physics prototype, the VFE was placed outside the active area with no particular
85 constraints in power consumption. It consisted of 30 layers of Si as active material alternated with

¹ For that reason the calorimeter systems at ILD will be placed inside the magnetic coil providing magnetic fields of 3.5 T

86 tungsten plates as absorber material. The active layers were made of a matrix of 3x3 Si wafers.
87 Each of these wafers was segmented in matrices of 6x6 squared pixels of $1 \times 1 \text{ cm}^2$. The prototype
88 was divided in 3 modules of 10 layers with different W depth per layer in each of these modules
89 (0.4, 1.6 and 2.4 X_0) making a total of 24 X_0 . Published results proving the good performance of
90 the technology and the PF can be found in references [12–17].

91 2 The SiW-ECAL engineering prototype

92 The new generation prototype is called the SiW-ECAL technological prototype and it addresses the
93 main technological challenges: compactness, power consumption reduction through power pulsing
94 and VFE inside the detector close to real ILD conditions. It will also provide data to deeply study
95 the PF and provide input to tune the Monte Carlo programs.

96 2.1 Silicon sensors

97 The sensors consist on float zone silicon wafers $320\mu\text{m}$ thick with high resistivity (larger than 5000
98 $\Omega\cdot\text{cm}$). The size of the wafer is $9 \times 9 \text{ cm}^2$ featuring an array of 256 PIN diodes of $5 \times 5 \text{ mm}^2$. A
99 MIP traversing the PIN parallel to its normal will create $\sim 80 h^+e^-$ pairs per μm which corresponds
100 to 4.1 fC if the particle traverses the $320\mu\text{m}$ perpendicularly to its larger surface.

101 The original design of the silicon wafers included an edge termination made of floating guard-
102 rings. It was observed in beam test[18, 19] that the capacitive coupling between such floating
103 guard-rings and the pixels at the edge was not negligible in tests with high energy beams (pions and
104 electrons with energies larger than 20-40 GeV). This coupling lead to fake events in which, at least,
105 the channels in the four edges of the wafer are triggered at the same time. This is why these events
106 are so often called squared events. An R&D program together with Hamamatsu Photonics (HPK
107 Japan) was conducted to study the guard-rings design as well as the internal crosstalk. As outcome
108 of this R&D program, the technological prototype is equipped with silicon wafers with:

- 109 • N wafers type-X with guard-rings of XXX characteristics (continuous, segmented, segmented
110 smaller??)
- 111 • N wafers type-Y without guard rings and the width of the peripheral dead areas lower than
112 $500 \mu\text{m}$ thanks to the use of stealth dicing technique.

113 For the wafers type-Y, the amount of squared events is expected to be reduced by, at least, a
114 factor XXX. In both cases, for interaction with low energy particles as the delivered at the DESY
115 beam test facility (see Section 4) the amount of squared events is expected to be negligible, therefore
116 we will not do any differentiation of our results depending on the wafer type mounted in the detector.

117 Is this needed? If so, what are the right plots to show? Before the assembly of the sensors in
118 the detector, these are characterized one-by-one by measuring the leakage current (of the order of
119 1 nA per single diode) as a function of the bias voltage (I-V curve), the full depletion voltage (of
120 40 V) extracted from C-V curve and the stability in time (leakage current versus time at a nominal
121 bias).

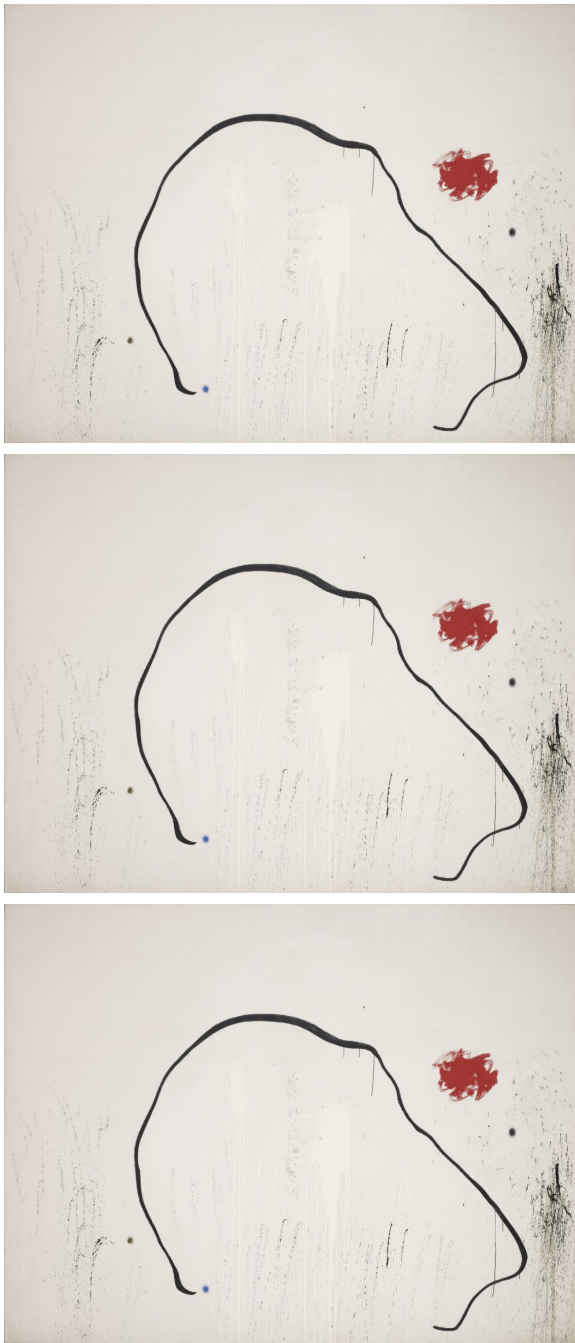


Figure 1. I-V curve, C-V curve, leakage current vs time. **Temporary picture:** La Esperanza del Condenado, J. Miró

122 2.2 SKIROC: Silicon pin Kalorimeter Integrated ReadOut Chip

123 SKIROC[20] (Silicon pin Kalorimeter Integrated ReadOut Chip) is the very front end ASIC designed
 124 for the readout of the Silicon PIN diodes. It consists of 64 channels in AMS 0.35 μm SiGe
 125 technology. Each channel comprises a low noise charge preamplifier of variable gain followed
 126 by two lines: a fast shaper for the trigger decision and a set of dual gain slow shaper for charge

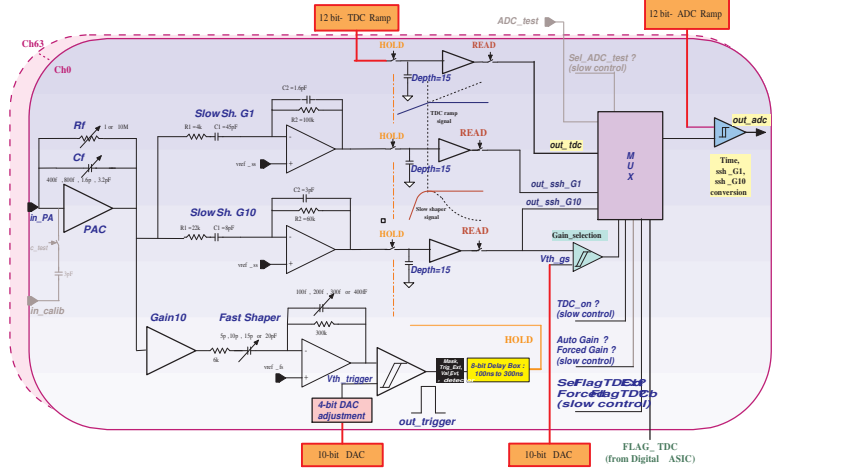


Figure 2. The schematics of the analog part of SKIROC2. High-stack picture (right bottom corner)

measurement. The gain can be controlled by modifying the feedback capacitance during the configuration of the detector. With the slowest gain, 6pF, the ASIC will handle a linear dynamic range from 0.1 to up to 1500 MIPs (a slightly less than the desired final value for the ILC). Finally, a Wilkinson type analogue to digital converter fabricates the digitized charge deposition that can be readout. Once one channel is triggered, the ASIC reads out all 64 channels adding a bit of information to tag them as triggered or not triggered and the information is stored in 15 cell deep physical switched capacitor array (SCA). The trigger threshold can be controlled both globally and locally (channel by channel) although the dynamical range for the channel by channel option is too small in the SKIROC version 2 due to a mistake in the development. The trigger holds the voltage of the two slow shapers with a tunable delay and also holds the voltage swept with the slow clock trigger to obtain timing information.

The SKIROC ASICs can be power-pulsed by taking advantage of the ILC spill structure: the bias currents of the ASIC can be switched off during the idle time between bunch trains. With this method, the ASIC is able to reduce its power consumption down to $25 \mu\text{W}$ per channel, meeting the ILC requirements. All the results shown in this paper are obtained using the power pulsing feature.

Every ASU of the SiW-ECAL prototype is equipped with 16 SKIROCs version 2. A new version, 2a, has been produced and will be used to equip new layers currently in production. In addition, a new generation of the ASIC, SKIROC3, is foreseen for the final detector construction. In contrast with SKIROC2/2a, the new ASIC will be fully optimized for ILC operation, *i.e.* full zero suppression, reduced power consumption etc.

2.3 Active Sensor Units

The entity of sensors, thin PCB (printed circuit boards) and ASICs (application-specific integrated circuits) is called Active Signal Units or ASU. An individual ASU has a lateral dimension of $18 \times 18 \text{ cm}^2$ and has glued onto it 4 silicon wafers (currently with a thickness of $320 \mu\text{m}$). The high voltage is delivered to the wafers using a HV-kapton sheet that covers the full extension of the wafers. The ASUs are equipped further with 16 ASIC for the read out and features 1024 square pads (64 per ASIC) of $5 \times 5 \text{ mm}$. The channels and ASICs are distributed along the ASU as shown in Figure ??

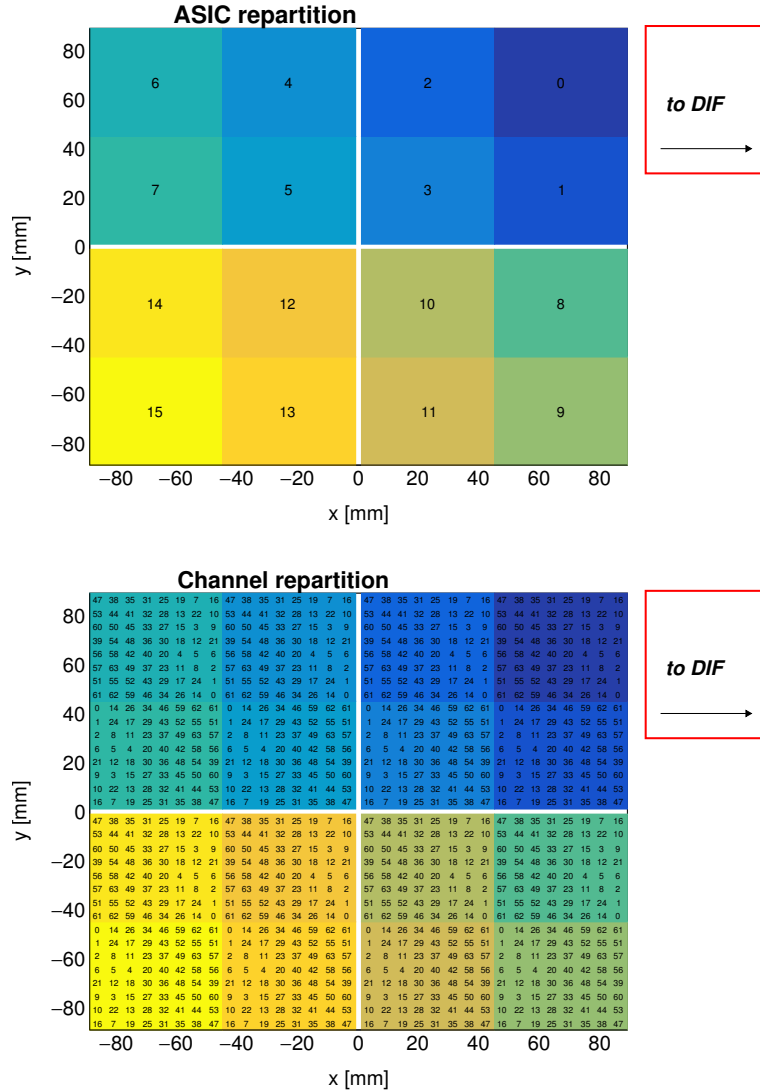


Figure 3. Repartition of the ASIC (up) and channels (down) in one ASU. In this perspective, the Si-Sensors are in glued in the back. The channels are separated (in x and y) by 5.5 mm. The empty cross in the middle of the ASU corresponds to the 1 mm separation between the sensors.

The readout layers of the SiW-ECAL consist of a chain of ASUs and an adapter board to a data acquisition system (DAQ) at the beginning of the layer. This adapter board is called SMBv4 and it also serves as a place to sit the power connectors (low voltage to power the analog and digital parts of the ASIC and high voltage to bias the PIN diodes) and the super capacitances used for the power pulsing. These capacitances of 400mF with 16 m Ω of equivalent serial resistance. The purpose of these capacitances is to provide local storage of the necessary charge to avoid the transport of current pulses over long cables, ensuring in this way the stability of the ASICs during the acquisition.

Currently, the technological prototype layers are built with version of PCB called FEV11 with 16 SKIROC (see Section 2.4). The FEV11 thickness is 1.6 alone and 2.7 mm including the ASICs in its current packaging: 1.1 mm thick LFBGA package. Figure 1 (left) shows a picture of a full



Figure 4. Left **Temporary picture: La Esperanza del Condenado, J. Miró:** Open single SLAB with FEV11 ASU, 16 SKIROC, interface card and DIF visibles. The silicon sensors are glued to the PCB in the other side. Right: two FEV11_COB boards with 16 SKIROC2a wire bonded. The ASICs are protected with watch glasses.

164 equipped short slab with FEV11 ASU. There are ongoing R&D activities in an alternative PCB
 165 design in which the ASICs are directly placed on board of the PCB in dedicated cavities. The
 166 ASICs will be in semiconductor packaging and wire bonded to the PCB. This is the so-called COB
 167 (chip-on-board) version of the ASU. A small sample of FEV11_COBs (same connexion pattern
 168 with the interface card than FEV11) with a total thickness of 1.2 mm has been produced and tested
 169 in the laboratory showing its readiness for tests with particle beams. A sample can be seen in Figure
 170 1 (right).

171 2.4 Data AcQuisition system

172 The design of the subsequent chain of the data acquisition (DAQ)[21] system is inspired by the
 173 ILC. Current DAQ consists of three modules which are designed to be generic enough to cope with
 174 other applications. The first module is the so called detector interface (DIF) which is placed at the
 175 beginning of each layer holding up to 15 ASUs. All DIFs are connected by single HDMI cables
 176 to the concentrator cards: Gigabit Concentrator Card (GDCC). The HDMI connection is used to
 177 transmit both slow control and data readout. One GDCC controls up to 7 DIFs collecting all data
 178 from them and distributing to them the system clock and fast commands. The most downstream
 179 module is the clock and control card (CCC). The CCC provides a clock, control fan-out of up to 8
 180 GDCCs and accepts and distributes external signals (i.e. spill signals).

181 The whole system is controlled by the Calicoes and the Pyrame DAQ software version 3 [22,
 182 23]. The Pyrame framework provides basic blocks (called modules) of control-command or data
 183 acquisition. Calicoes is specific the implementation of these blocks for control-command and data
 184 acquisition of the SiW-ECAL prototype. This new version of the DAQ software implements a new
 185 mechanism to allow any module to treat and publish data in real time. Those data are made available
 186 to any requesting module, in particular to a new online monitor module developed for this beam
 187 test, allowing for quick online checks of the data quality and integrity.

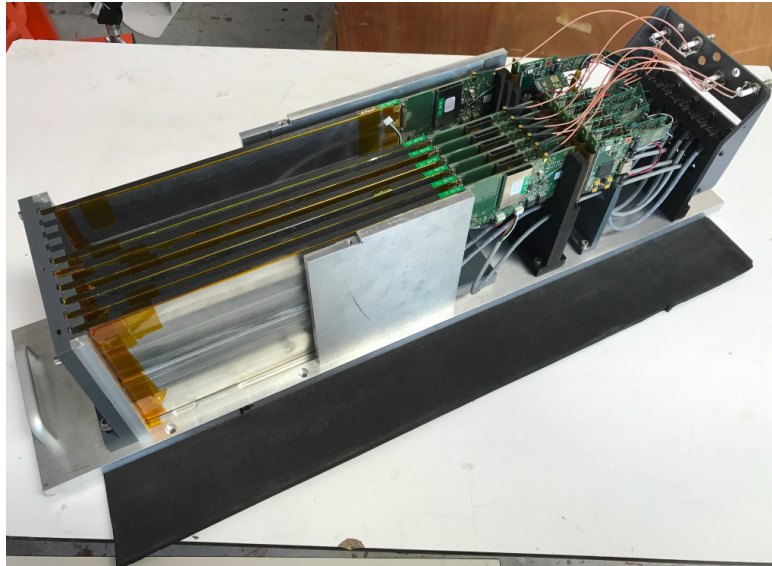


Figure 5. Prototype with 7 layers inside the aluminum stack.

188 2.5 Setup

189 The prototype tested in beam is composed of 7 layers consisting in one short SLAB each. A short
 190 SLAB is made of: one single ASU FEV11 equipped with 16 SKIROC2 and 4 wafers glued on the
 191 other side (1024 channels); an interface card SMBv4; and a DIF. All these elements sit on a "U"
 192 shape carbon structure to protect the wafers. The full system is then covered by two aluminum
 193 plates to provide electromagnetic shielding and mechanical stability. The 7 layers are supported by
 194 a PVC and aluminum structure that in which can be inserted to 10 layers. The distance between
 195 two layer slots is 15 mm and this space is used to place tungsten plates of different thicknesses. For
 196 the beam test described in Section 4, the layers were placed in positions 1-6 and 10. During the
 197 commissioning, the slabs have been tested both inside and outside of the structure. A photograph
 198 showing the prototype can be seen in Figure 5. The ASICs and channels are labeled with numbers
 199 following design and DAQ criteria: from 0-16 in the case of the ASICs and from 0-63 in the case
 200 of the channels.

201 3 Commissioning of the detector

202 This beam test was prepared by a careful and comprehensive commissioning comprising: the debug
 203 of the single SLABs with special emphasis in the control of the noise and the study of the prototype
 204 performance in cosmic rays tests.

205 The SKIROC2 has been already commissioned for previous experiences (see for example
 206 the references [24, 25]). Therefore, all the settings used for the SKIROC2 to obtain the results
 207 described in this paper are motivated by previous experiences. For example, the value of 1.2pF
 208 for the preamplifier. With this gain, the SKIROC2 ensures a linearity better than 90% for 0.5-200
 209 MIPs, which is optimal for electromagnetic showers created by few GeV electrons or positrons.
 210 The delay of the trigger signal is the same than in reference [24, 25]: 130 DAC for all ASICS. This

211 value was chosen by selecting the delay in which an injected signal of few MIPs of value get the
212 maximum value of ADC.

213 3.1 Optimization of noise levels

214 The purpose of this phase was to monitor and control the noise levels of the prototype. The
215 commissioning includes the definition of trigger threshold values and a list of noisy channels to be
216 masked. Studying and control the noise levels in an self-triggered and high-granularity calorimeter
217 is crucial since noisy channels may saturate the DAQ faster than physical signals. Two different
218 types of noise were identified: randomly distributed (in time) noisy channels and noise bursts
219 affecting to all layers at the same time.

220 The first type of noise source (randomly distributed in time) forced us to define a list of channels
221 to be masked in all layers. Again, two different type of noisy channels have been identified. The
222 first group is composed by randomly distributed (in space) channels which slightly larger number
223 of triggers than the others. The second group is made of a fixed list of channels, all in the same
224 positions for all SLABs, that were giving underflowed ADC triggers at high rates.

225 The channels associated to "underflowed-noise" events were identified by means of the online
226 monitoring tools. Some preliminary inspections of the FEV11 layout hint that the cause of this
227 "underflowed-noise" events may be in an improvable routing of the lines from the PIN pad to the
228 SKIROC. For this reason, if a given channel appeared to be associated to "underflowed-noise"
229 events in one of the SLABs, it was masked in all of them, taking in this way the most conservative
230 solution. For example, all channels number 37 were masked in all ASICs. More studies in this
231 respect are to come.

232 The list of the noisy channels randomly distributed in time and space was defined by means of
233 dedicated data taking runs. These runs were characterized by: their short acquisition windows (of
234 2.5 ms, only 1.1 ms of effectively data taking time), their low spill frequency (5 Hz) to minimize the
235 chances of having real events due to cosmic rays hitting the detector during the data taking; and the
236 relatively high trigger threshold values between 250 and 400 DAC (which is equivalent to \sim 0.5-2
237 MIP, see Section 3.2 for more information). The full process was an iterative process starting with
238 several repetitions of runs at a high threshold value and then some iterations at lower threshold each
239 up to 250 DAC. In every of these iterations, the channels identified as noisy were masked. A full run
240 involved 3-5 threshold values and at least two repetitions per value. Again, we decided to follow a
241 conservative approach for list the noisy channels to be masked: if the channel was triggered at rates
242 larger than 0.5-1% of the total number of triggers it was added to the list.

243 In addition to the different noisy channel types described above, we also have masked full
244 sectors of the SLABs if an ASIC was faulty (at least 70% of channels listed as noisy) or if a Si-wafer
245 was misworking (high leakage currents). In these cases and in all mentioned above, the masking
246 involved two steps: disabling of the trigger and the disabling of the power of the preamplifier of
247 that channel. A summary of the results of the masking procedure is shown in Figure 6.

248 We observed that the noise bursts happening coherently at the same time in all SLABs was
249 associated to cases when the electrical isolation between SLABs was broken. This is a hint of
250 a system effect as grounding loops or noise in the power supplies. The issue was circumvented
251 by improving the electrical isolation of single layers. We have also observed that the noise burst
252 happen only at the end of long acquisitions therefore, in addition to the improved isolation, we

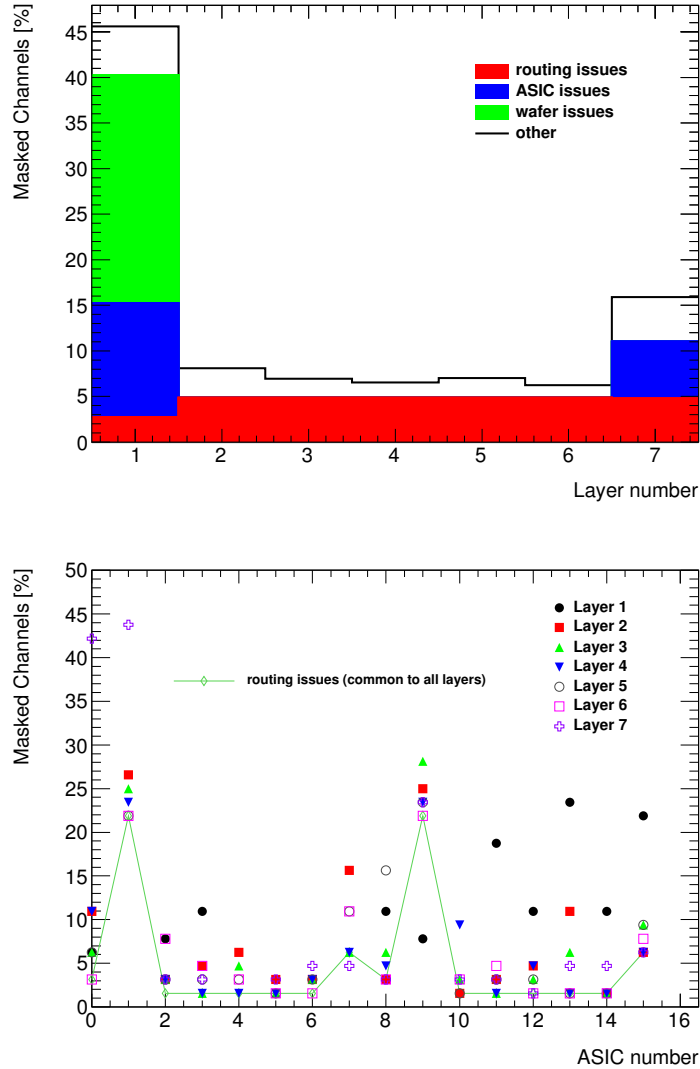


Figure 6. Ratio of channels that are marked as noisy in all slabs. Top: inventory of the different type of noisy channels per slab. Bottom: break up of the noisy channels per ASIC. We see two spikes in the number of channels masked due to routing issues in the ASICs 1 and 9. These two ASICs are located near the SMB where the density of lines (data and power transmission) is higher, complicating in this way the routing. The ASICs 4-7 (wafer issue) and 10 from layer 1 and the ASIC 4 from layer 7 are not included in the second plot since they are fully masked.

253 selected short enough acquisitions windows (which indeed are the most appropriate to the high
 254 rates of particles in the DESY beam). However, more studies in the laboratory are needed in order
 255 to fully understand these issues.

256 3.2 Threshold determination

257 Once that the SKIROC main settings have been fixed and the masking of the noisy channels at a
 258 relatively high threshold value has been done, the final step is the selection of the optimal trigger

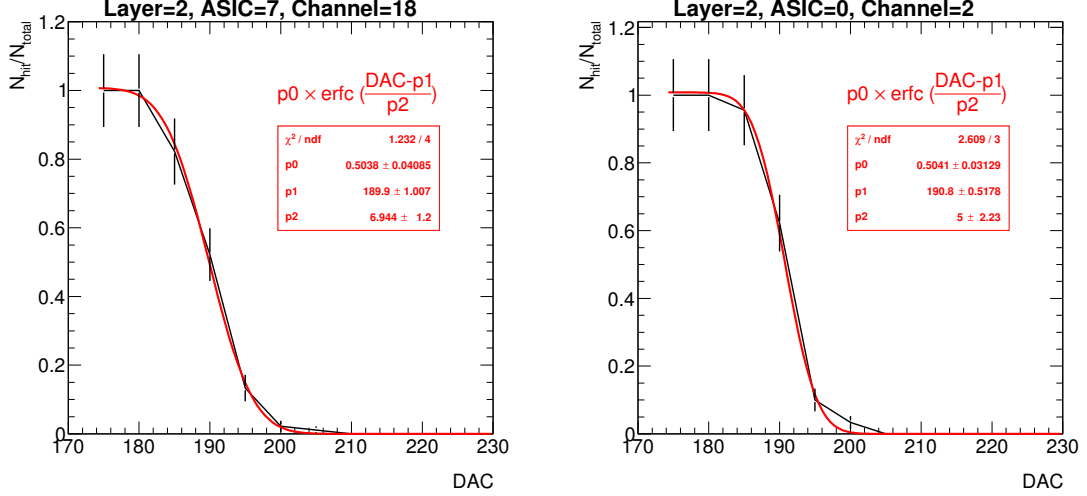


Figure 7. Two S-curves obtained during noise runs.

threshold values. For that, we perform dedicated runs in which we scan a reasonable range of trigger threshold values (in DAC units) with all channels enabled (excepted the marked as noisy). For each of the DAC points we took data during ~ 1 minute per DAC in order to speed up the commissioning. Plotting the total number of hits normalized to the maximum vs the DAC for each channel gives the so-called S-curves. In the absence of external signals (cosmic rays, injected signals, etc) these noise S-curves show the convolution of the envelope of the electronic noise at the output of the fast shaper (the trigger decision line). Indeed, the size of this enveloppe is related to slow clock frequency (larger periods, larger possibility to find a noise variation over the threshold).

To reduce to the minimum the presence of cosmic rays signals, we perform runs with short open acquisition windows (1.1 ms). In Figure 7 two S-curves of two different channels from the second layer of the setup are shown.

The S-curves are fitted to a complementary error function

$$S(DAC) = p_0 \times erfc\left(\frac{DAC - p_1}{p_2}\right) = \frac{2p_0}{\sqrt{\pi}} \int_{\frac{DAC-p_1}{p_2}}^{\infty} \exp^{-t^2} dt, \quad (3.1)$$

where p_0 is 1/2 of the normalization, p_1 is the value in which the noise levels are the 50% of its maximum and p_2 give us the width of the S-curve.

The function from equation 3.1 was fitted to all channels data and all the values of p_1 and p_2 were saved. To decide the final trigger threshold value for the full ASIC, we took the maximum between:

$$DAC_{optimal}^{ASIC-j} = \langle p_1^{ASIC-j} \rangle + 5 \times \langle p_2^{ASIC-j} \rangle \quad (3.2)$$

and 230 if more than the 30% of the 64 channels S-curves in the ASIC could be fitted. If not, we took a most conservative value of 250 DAC. The election of these two values was sustained by previous experiences, see for example [24].

The optimal trigger threshold values for all ASICs are shown in Figure 10.

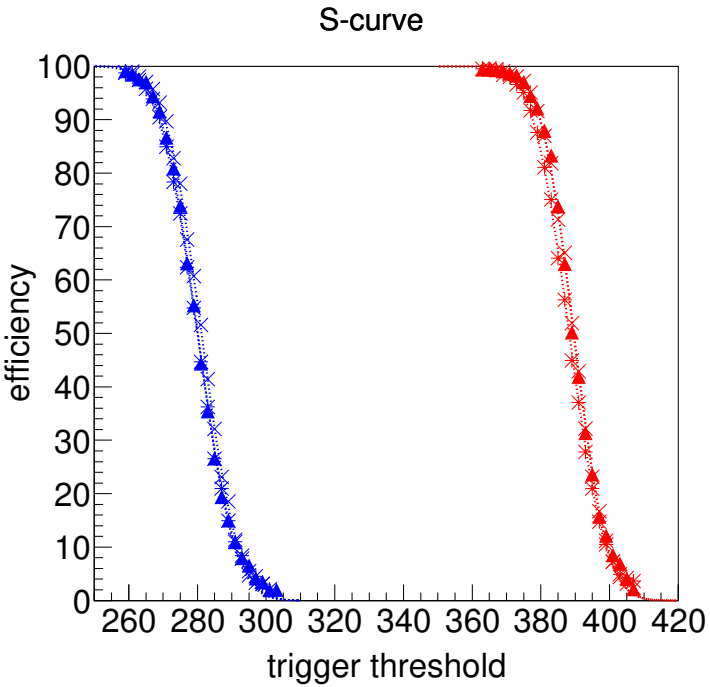


Figure 8. S-curves with charge injection (1 MIP in blue and 2 MIPs in red) for two different channels in a SKIROC2 testboard. From this plot, we extract a $S/N = 12.8$ in the trigger line.

280 3.3 S/N ratio in the trigger line

281 Similar kind of measurements can be done but using external signals. This will allow to calculate
 282 the signal over noise (S/N) ratio to trigger 1 MIP signals. To calculate the S/N of the trigger we need
 283 to compare the 1 MIP S-curve and 2 MIP S-curve. The S/N will be defined as the ratio between the
 284 distance of both S-curves at its 50% and the width of the S-curve.

285 In Figure 8 we see the 1 MIP and 2 MIP S-curves obtained for a one channel in a SKIROC
 286 testboard in which a single SKIROC2 in BGA package is placed and the 1 MIP and 2 MIPs "fake"
 287 signals are directly injected in the preamplifier (via a 3 pF capacitor in the injection line). From
 288 this plot we can extract a S/N ratio of ~ 12 . We don't expect large differences with the results that
 289 we would obtain with full equipped SLABs although this board is thought for commissioning and
 290 test of the SKIROC ASICs in an "ideal" environment in contrast with the FEV ASUS that are
 291 optimized to meet detector constraints and to hold several ASICs at the same time. For example:
 292 only power pulsing of the analog power is done in this testboard, there is a set of external capacitors
 293 on the board connected to some ASIC pins and usually only one channel is tested. This allows us
 294 to commission the SKIROC2 itself

295 We have obtained similar results using real signals, in this case cosmic rays signals. This is
 296 shown in Figure 9 where we show the result of the fit to the noise S-curves for all channels (in red)
 297 in one of the ASICs of the second layer together with the results of the S-curve with cosmic rays
 298 (black points and blue line). For the cosmic S-curve we took 30 min of data per point using very
 299 long spills (150 ms) in frequencies of 5Hz and we add up the triggers from all channels together.
 300 In addition, using the knowledge of the MIP value (see next section), we performed a simple cut

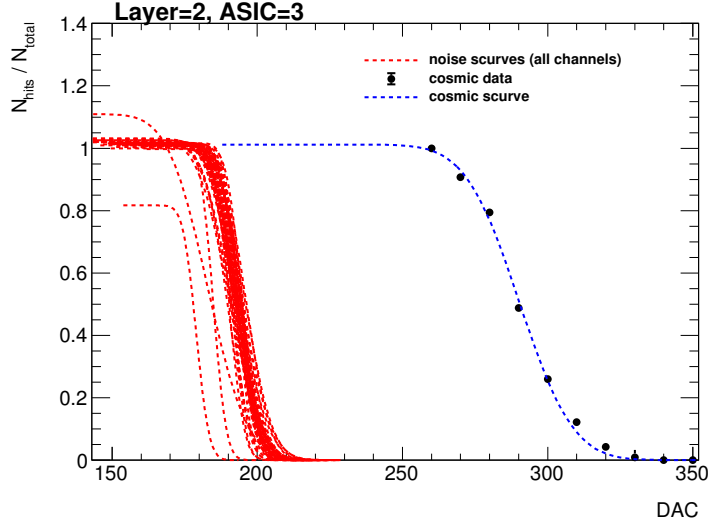


Figure 9. S-curves for noise (channel by channel, only the result of the fit) and cosmic rays (all channels together) for one ASIC in layer 2.

in the ADC to keep only signals corresponding to a MIP (pedestal subtracted) ± 30 ADC counts. With this cut we try reduce the contribution of muons traversing the wafers with very large angles but we don't have a way to select perpendicular tracks since we were using simple setups with only single slabs during in the run. For all these reasons, we expect a broader distribution of the cosmic S-curve. This is one of the reasons why, if we calculate the S/N using this plot, the value would be unrealistic (much lower, indeed). In addition to this, we should remember that the noise S-curve do correspond to the real noise distribution but only to the envelope of the noise in the fast shaper, therefore the distance between the two S-curves is smaller than the real distance between noise and signal.

In conclusion, both ways of estimating the S/N ratio of the trigger have their own limitations but in both cases, the 50% of the S-curve of 1 MIP are compatible within ± 10 ADC. This allow us to, at least, estimate the relative distance between our final trigger threshold for every ASIC and the 1 MIP position. This is shown in Figure 10. Two ASICS ($\sim 2\%$) have a trigger threshold value of 0.67 MIP. The 11% of the ASICS have a trigger threshold between 0.5 and 0.55 MIP and the rest, 87%, have trigger thresholds slightly lower 0.5 MIP.

3.4 Prospects

All the commissioning procedure described above relies in very conservative decisions due to the presence of unknown noise sources during most of the commissioning phase. These sources are now well known and isolated and therefore a new "noise" commissioning procedure can be proposed for the next beam test. It will consist in an iterative algorithm that first will identify and mask the "underflowed-noisy" channels and afterwards run a set of acquisitions in which the number of triggers per channel will be compared with the number of expected triggers assuming only cosmic rays as signal. This will allow us to have an unambiguous definition of the noise levels channel per channel instead of defining that levels relatively to the total number of recorded triggers. Finally,

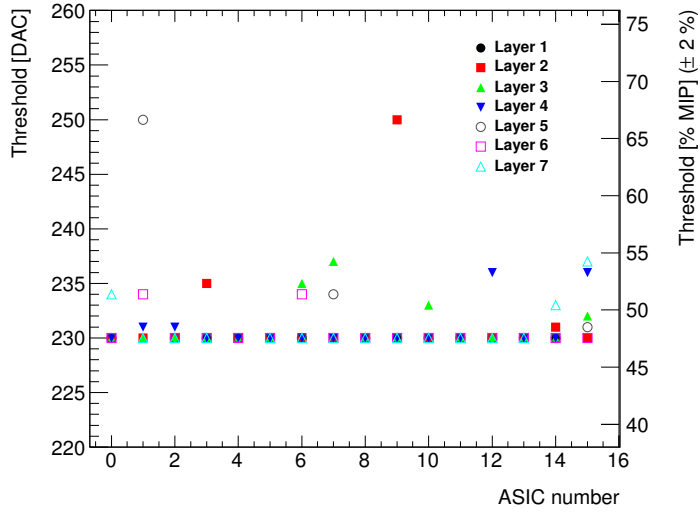


Figure 10. Summary of trigger threshold settings for all ASICs in the setup. The values are given in DAC and in estimated MIP units, using the distance between two MIPs from Figure 8. The uncertainty quoted in the right axis is estimated from difference between the 50% position of the S-curve for one MIP extracted from this figure and Figure 9.

once that the noisy channels are identified, the optimization of the threshold levels will be performed and the last run for identification of noisy channels will be taken using this optimal level will be taken. In this run, we can decide to mask the noisy channels or to increase its own trigger threshold level if we are using Skiroc2a.

Using this new procedure we manage to reduce the number of masked channels by a factor 2 without any loss of performance, at least in the laboratory and using 3 of the 7 SLABs. This new procedure will be tested in the next beam test. Also, in order to optimize the commissioning of the detector, we will propose a new set of measurements in the next beam test consisting in: a scan of optimal delay of the hold values of the trigger using MIP like particles; and a threshold scan for the determination of the S/N in the trigger line using 1 MIP and $\sqrt{2}$ MIP (tilting the detector by 45 degrees) signals.

4 Performance on positron beam test at DESY

The beam test line at DESY provides continuous positron beams in the energy range of 1 to 6 GeV with rates from few hundreds of Hz to few KHz with a maximum of ~ 3 KHz for 2-3 GeV. These positrons are produced in the following way: first, the electron/positron synchrotron DORIS II is used to produce a photon beam via bremsstrahlung when interacting with a carbon fiber target; secondly, these photons are then converted to electron/positron pairs; and, finally, the beam energy is selected with dipole magnets and collimators. In addition, DESY gives access to a bore 1 T solenoid, the PCMag.

The prototype tested in beam in June 2017 consisted of 7 layers as explained in Section 2.5. The detector was exposed to a positron beam in the DESY test beam area (line 24). By means of an

346 external pulse generator we defined the length of the acquisition window to be 3.7 ms at a frequency
347 of 5 Hz, emulating in this way similar conditions than the ILC will have. The detector was running
348 in power pulsing mode without any extra active cooling system.

349 The physics program of the beam test can be summarized in the following points:

- 350 • Commissioning and calibration without tungsten absorber using 3 GeV positrons acting as
351 minimum ionizing particle (MIPs);
- 352 • magnetic field tests up to 1 T in the PCMag;
- 353 • response to electrons with fully equipped detector, i.e. sensitive parts *and* W absorber.

354 For the first two points from above, we used the SiW-ECAL in the tracker mode, *i.e.* without
355 intercalated tungsten plates. Due to the low material budget of our setup when the tungsten is
356 not included, a beam of positrons of few GeV of energies provides satisfactory data for calibration
357 since the positrons deposit the minimum amount of energy by ionization. The calibration of the
358 detector was realized by directing the 3 GeV positron beam on 81 positions equally distributed over
359 the surface of the detector. These data were used for pedestal estimation and energy calibration.
360 Calibration and pedestal analysis was done for all single layers not requiring track reconstruction.
361 The study of these data is discussed in Section 4.1 for the pedestal and noise studies and Section
362 4.2.1 for the results of the calibration.

363 For the tests inside the magnetic field, a special PVC structure was designed and produced
364 to support one single SLAB. The purpose of such test was twofold: first to prove that the DAQ,
365 all electronic devices and the mechanical slab itself were able to handle strong magnetic fields;
366 second to prove the stability of the performance during these tests. We took several runs, with 0, 0.5
367 and 1 T magnetic fields with and without 3 GeV positron beam and we observed that the pedestal
368 and noise values are independent of the magnetic field (see Section 4.1.1). The study of the MIP
369 calibration stability will be discussed in future publications, where full studies of the data including
370 comparison with simulations should be included.

371 To fulfill the last point of the list we inserted W plates of different thicknesses between the
372 sensitive layers. Then we performed a scan of energies of the positron beam: 1-5.8 GeV. We
373 tested the response of the detector with three different configurations of the W repartition. The
374 accumulated amount of tungsten, in radiation length units, X_0 , in front of each of the SLABs is:

- 375 • W-configuration 1: 0.6, 1.2, 1.8, 2.4, 3.6, 4.8 and 6.6 X_0
- 376 • W-configuration 2: 1.2, 1.8, 2.4, 3.6, 4.8, 6.6 and 8.4 X_0
- 377 • W-configuration 3: 1.8, 2.4, 3.6, 4.8, 6.6, 8.4 and 10.2 X_0

378 Preliminary results of the raw electromagnetic shower profiles look promising but will not be
379 discussed in this article since deeper analysis and comparison with montecarlo simulations will be
380 needed to extract conclusive results from the data. This will be the topic of a future article, possibly
381 combining data with future beam tests that are currently in preparation. What it is included in this
382 article, in Section 4.3 is the study of the pedestals in this events.

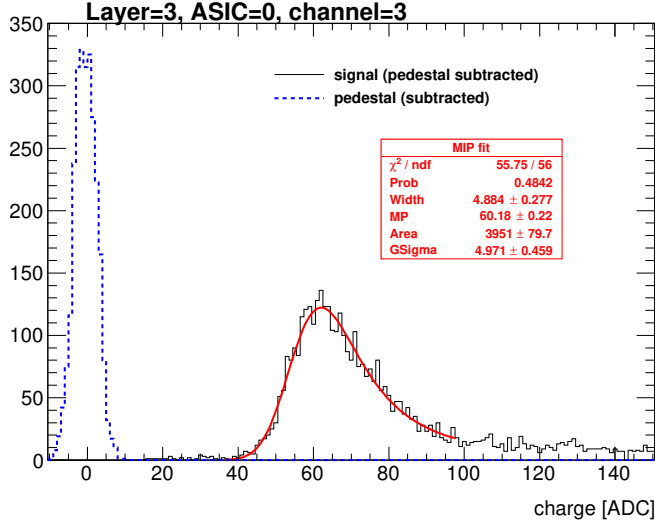


Figure 11. Pedestal (blue dashed line) and signal (black continuous line) distribution for one channel in the third layer. The results of the MIP calibration fit are included (red). The pedestal distribution is shown only for the first SCA to keep the y-axis within a reasonable range. The signal distribution is integrated over all SCAs.

383 4.1 Pedestal and noise studies with the SiW-ECAL in tracker mode

384 Due to the way that the SKIROC2 ASICs work, it is possible to extract the pedestals simultaneously
 385 to the recording of signals from particle interactions. Indeed, when a channel is triggered, the rest
 386 are read out at the end of the slow clock period (usually called BCID - for bunch crossing ID and
 387 marked as non triggered channels. This allows us to reconstruct the pedestal distribution for all
 388 channels and for all SCAs. These distributions are fitted with a Gaussian and the pedestal value
 389 are associated with the mean of the result of the fit. These values will be, afterwards, subtracted
 390 to the ADC recorded by the SKIROC2 for all channels and SCAs. The noise of the channel and
 391 SCA corresponds to the width of the pedestal distribution. The calibration runs have been used to
 392 calculate the pedestal distribution reference values of the detector. In Figure 11 we show the signal
 393 and pedestal distribution of a single channel after subtracting the pedestal mean position.

394 In Figure 12 (left) we observe that both the pedestal position for each SCA in the same channel
 395 can be different in few %. In the case of the pedestal mean position, these differences are even larger
 396 between different ASICs in the same layer (Figure 13, left plot) or between layers (Figure 14, left).
 397 This is the reason of performing the pedestal correction layer-, chip-, channel- and SCA-wisely. For
 398 the noise, the dispersion is smaller (~ 5%) and only dependent on the SCA. This is shown in the
 399 right plots of Figures 12, 13 and 14.

400 4.1.1 Pedestal and noise in large magnetic fields

401 For the tests inside the magnetic field we used the SLAB of the first layer in the special PVC struture
 402 mentioned at the begining of this section. We should also mention that the PCMag is in a different
 403 area (downstream) on the same beam line, therefore, due to the presence of additional collimators
 404 the beam rates are lower.

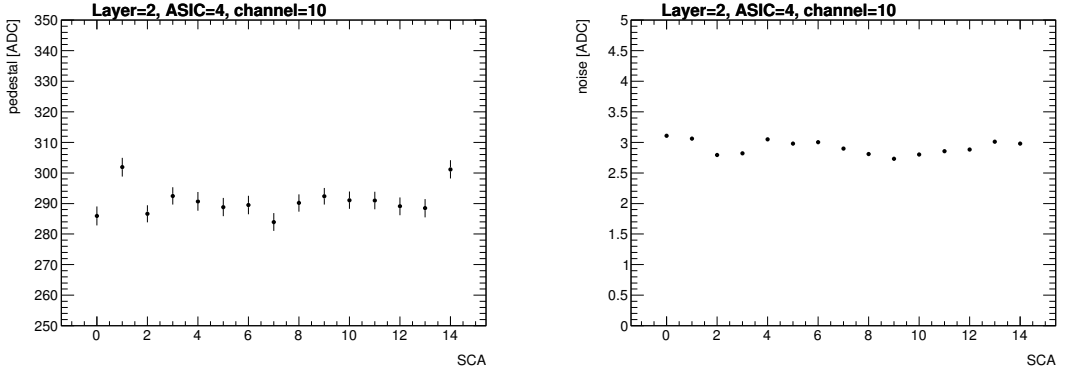


Figure 12. Pedestal mean position (left) and width (right) for one channel in the second layer.

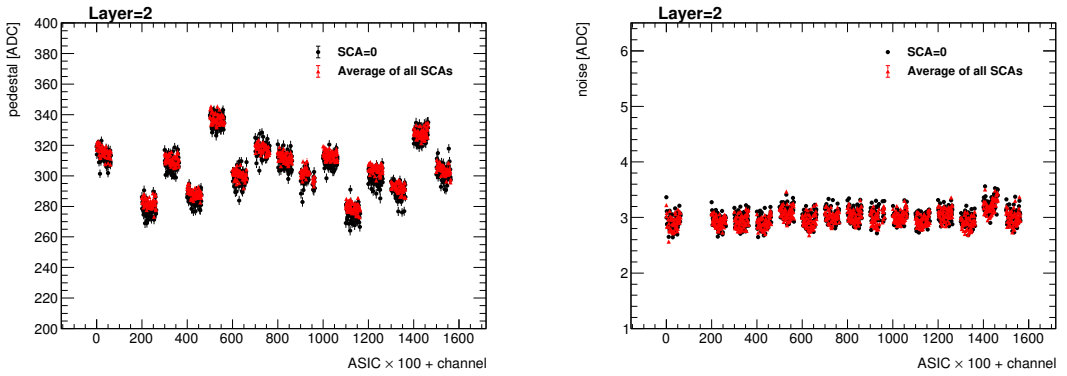


Figure 13. Pedestal mean position (upper plot) and width (lower plot) for all channels in one layer. The data is grouped on bunches in which the value in the x-axis corresponds to the value of the channel number plus the value of the ASIC number multiplied by 100. The black points show the value for the first SCA and the red points show the average value for all the others SCAs (with the standard deviation of the sample as error bar).

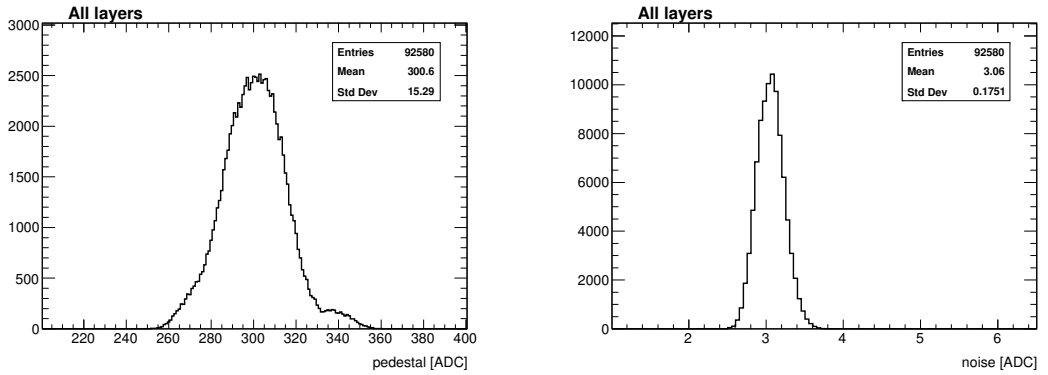


Figure 14. Pedestal mean position (left) and width (right) for all channels and all SCAs in the setup.

405 We divided the data taking in 3 stages in this order: a long run (13h) with a magnetic field of
 406 1 T, a second and shorter run of 3 hours with 0.5 T and a final run with the magnet off. In the cases

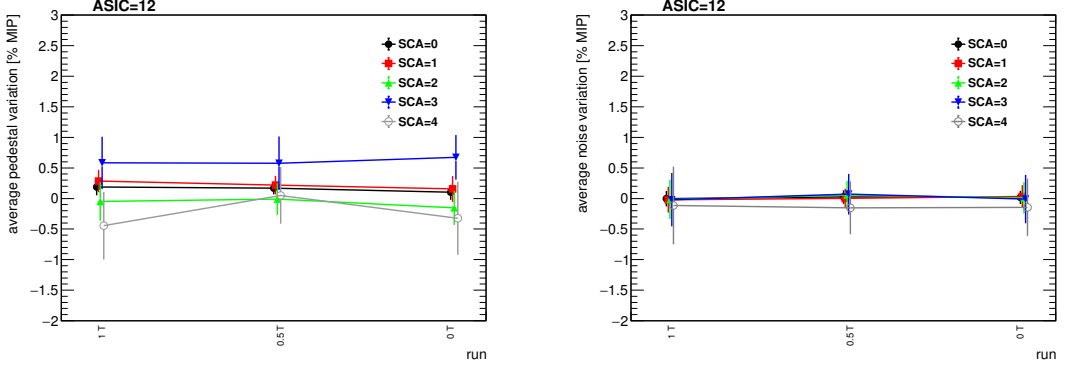


Figure 15. Average deviation of the pedestal mean position (left) and width (right) for all channels in the ASIC 12. The values are given in MIP units obtained from calibration (see Section 4.2.1).

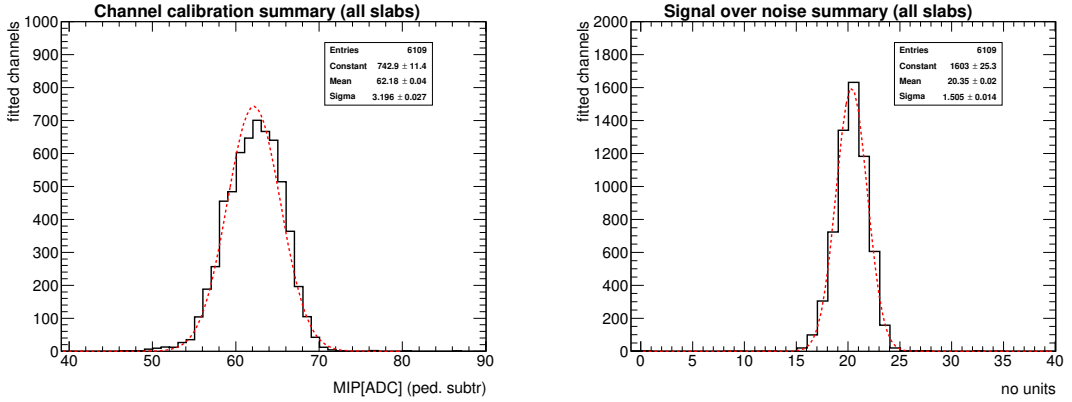


Figure 16. Result of the MIP position calculation and signal over noise calculation for all calibrated channels.

were we had beam, we used the 3 GeV positron beam settings impacting in the ASIC number 12.

The comparison of the pedestal values and noise levels between the reference run in the stack and the different runs in the magnetic field are shown in Figure 15. We see that in both cases, the agreement is perfect within the statistical uncertainties. Due to the lower rates in this beam area, the analysis is only done up to few SCAs.

4.2 MIP response and tracking efficiency with the SiW-ECAL in tracker mode

After the calculation of the pedestals for each channels and SCA, these are subtracted and the same data (without track recognition) are used for the calibration. A Landau function convoluted by a Gaussian is fit to the resulting hit distribution in ADC units. The most-probable-value of the convoluted function is taken as the MIP value, allowing thus for a direct conversion from ADC to energy. We have obtained a raw energy calibration spread of the 5% among all channels with the 98% of all available channels being fitted. Results are summarized in figure 16, leftmost plot.

We checked the MIP calibration by selecting tracks that cross the detector parallel to its normal and filling a histogram with the energy measured by each channel with a hit. We did this for all calibration runs together. The results are shown in figure 17 where the single channel

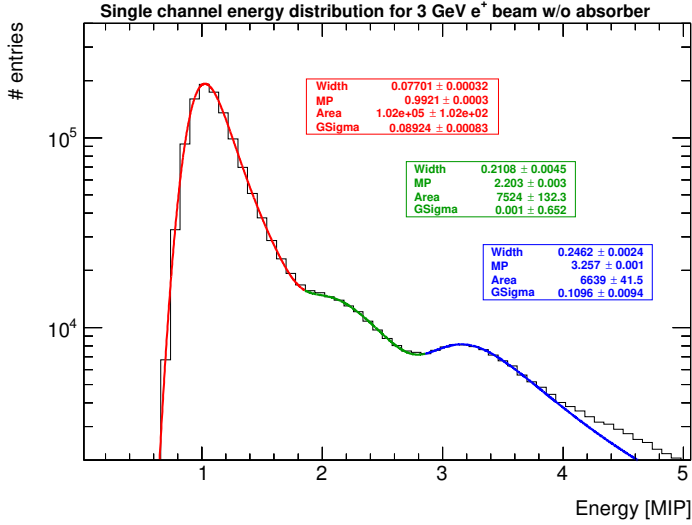


Figure 17. The single channel energy distribution (for all calibrated channels) for 3 GeV positron tracks acting as MIPs.

422 energy distribution for MIPs is shown for all calibrated channels in the same distribution. The
 423 distribution nicely fits in the 1 MIP spectrum, showing in that way the good performance of our
 424 default calibration that, for simplicity, was done without requiring tracking reconstruction. The
 425 distribution also reveals the presence of a second and third peak due to events involving multiple
 426 particles crossing the detector.

427 To evaluate the single hit detection efficiency we define a high purity sample of events of
 428 positrons traversing the detector perpendicularly by selecting tracks with at least 5 layers (of 7
 429 possible) with a hit in exactly the same channel. Afterwards we check if the other layers have or
 430 not a hit in the same channel (expanding the search to the neighbor channels) with energy larger
 431 or equal than 0.3 MIP. Finally, we repeat this for all layers and channels. The results are shown in
 432 Figure 18. Except few exceptions, the efficiency is compatible with 100%. Lower efficiencies in
 433 the first layer are related to the presence of noisy channels not well identified in the commissioning
 434 phase that boosted the filling of the the 15 SCAs of three ASICs. In the last layer (separated from the
 435 other layers by four slots of 1.5 cm instead of only one) we also observe few small deviations from
 436 the ~ 100% which are indeed associated to a slight misalignment of the tracks visible only in the
 437 outliers channels. If we remove these channels i nthe outliers from the analysis the full efficiency is
 438 recovered.

439 4.2.1 S/N ratio in the ADC

440 The signal-over-noise ratio in the ADC (corresponding to the slow shaper of the SKIROC2) is
 441 defined as the ratio between the most-probable-value of the Landau-gauss function fit to the data
 442 (pedestal subtracted) and the noise (the pedestal width). This quantity has been calculated for all
 443 channels and all slabs and, in average, it corresponds to 20.4. Results are summarized in Figure 16,
 444 rightmost plot.

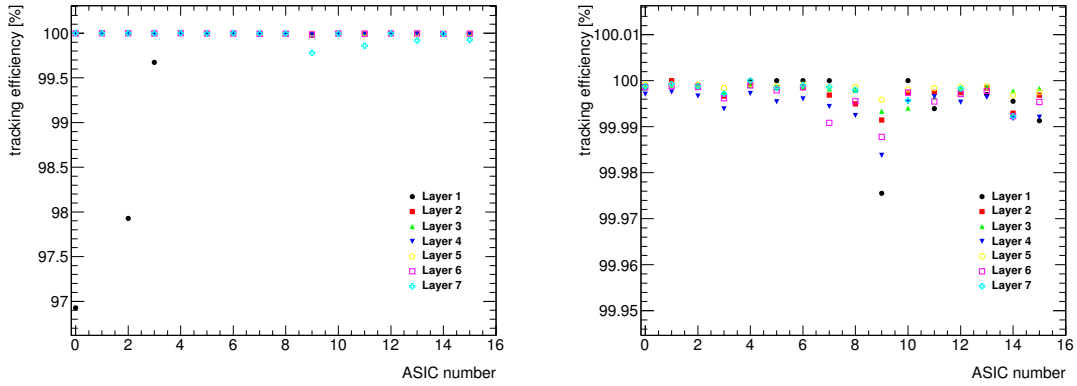


Figure 18. Left: MIP detection efficiency for all layers and ASICs in high purity samples of tracks of MIP-like acting particles. Right: same figures with a zoom in the y-axis. In both cases, the average efficiency of the 64 channels in each ASIC is shown.

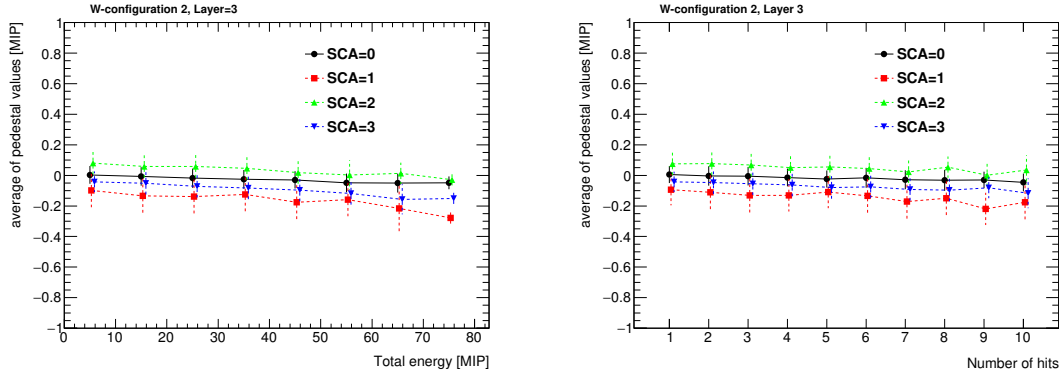


Figure 19. Left: mean position of the projection of the pedestal distribution of all channels of ASIC 12 in the Layer 3 calculated when different energies are collected in the ASIC (in bins of 10 MIPs). Right: same but as a function of the number of hits. In both cases, the results are shown for few SCA. The points for SCA larger than zero are slightly shifted in the x-axis to optimize the visualization.

445 4.3 Pedestal stability in electromagnetic shower events

446 The pedestal stability in events with large amount of charge deposited by the ASICs, as are the
 447 electromagnetic shower events, has been also calculated. All the results shown in this section
 448 correspond to data taken during the tungsten program, using the W-configuration number 2 when
 449 shooting the beam in the ASIC 12 (and partially in the 13). Only the ASIC 12 is used in the
 450 analysis. For other configurations and positions of the beam we get comparable results. We used
 451 also a calibrated data sample where the pedestal values have been subtracted and the MIP calibration
 452 has been applied. Therefore, all energy measurements are given in MIP units and the pedestal
 453 values are expected to be equal to zero. In order to select a high purity of electromagnetic shower
 454 like the events, we used a simple criteria: select only events with at least 6 of the layers with at least
 455 a hit with $E > 0.5$ MIP.

456 Two main observations have been extracted from the recalculation of the pedestals and its

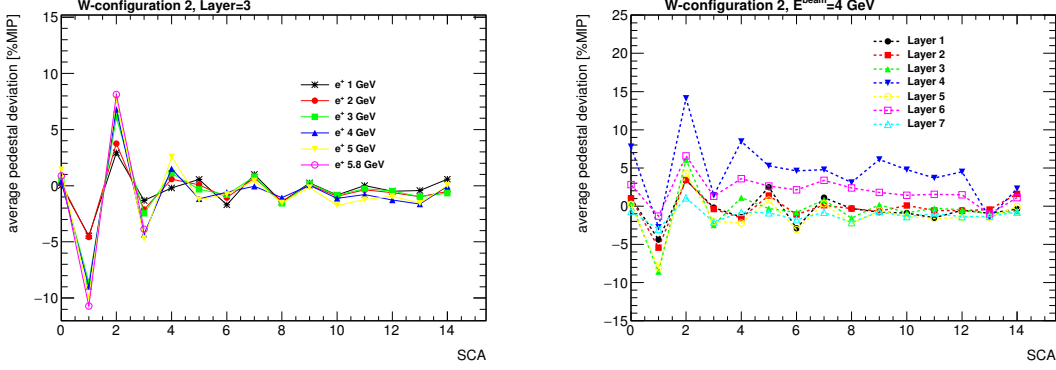


Figure 20. Left: average value on each SCA of the calculated pedestals for all channels of ASIC 12 in the Layer 3 for different energies of the beam. Right: same but fixing the energy of the beam and comparing several layers.

457 comparison with the values obtained previously during the calibration runs. The first observation
 458 consists in a relatively small drift of the pedestal values towards lower values when the collected
 459 energy is high (or when the number of triggered channels is large). For events with 80 MIPs
 460 collected in the ASIC, we have an average drift of ~ 0.05 MIP. This can be seen in
 461 Figure 19 for several SCAs where the average of the projection of the pedestal distribution for all
 462 channels non triggered in ASIC 12 of layer 3 is plot as a function of the total energy measured by
 463 the ASIC (or the total number of hits). We see that in all cases, the slopes of the curves for each
 464 SCA are very similar. This is feature is known and it is due to the architecture of the SKIROC2
 465 (and 2a) ASICs where high inrush of currents can slightly shift the baseline of the analogue power
 466 supply. This feature is foreseen to be removed from the SKIROC3 ASICs.

467 The second observation extracted from this analysis can be also seen in Figure 19: in addition
 468 to the small drift of the pedestal value an SCA-alternate global shift is observed. This feature is
 469 still not fully understood although the fact that the effect is observed in alternate SCAs but no time
 470 dependence has been observed hints to some issue affecting the digital part of the ASIC (where the
 471 SCAs enter in play). In Figure 20 we can see the effect, SCA per SCA, for different energies of the
 472 beam and for different layers. We see that the effect is enhanced when large amounts of charge are
 473 deposited in the ASIC (*i.e.* at larger beam energies or for the layers in the maximum of the shower
 474 profile). Dedicated tests in the laboratory and in the beam are needed in order to clarify this issue.

475 4.4 Fake triggers filtering

476 Several types of fake signals have been observed in the technological prototype since its construction
 477 and test. A detailed description of them can be found in previous articles, as for example, in Ref.
 478 [24]. All these fake signals are easily identified and tagged during the data acquisition and removed
 479 afterwards from the analysis not introducing any loss of performance as can be seen, for example,
 480 in the tracking efficiency plots. In the following, we briefly describe the status of the monitoring,
 481 debugging and filtering of such kind of events.

482 **Empty triggers**

483 Empty trigger events are a well known feature of SKIROC2. The issue appears when during the
484 acquisition the rising edge of the slow clock falls during the OR64 signal used to signalize the
485 lecture of a signal over threshold to validate the change to a new SCA. When this happens at the end
486 of the clock period, the change to a new SCA is validated twice. This effect creates around 10-15%
487 of empty events which are easily filter and removed from the analysis. **The ratio of empty triggers**
488 **in the new SKIROC2a is reduced to ~ 3% by reducing the length of the OR64 by a factor X.**

489 **Plane events and retriggers**

490 Another well know issue is related to the appearance of bunches of consecutive fake triggers that
491 quickly fill several SCA in consecutive slow clock periods. These events are also characterized by
492 triggering many channels (some times even all channels of an ASIC) at the same time. Although the
493 ultimate reason of the appearance of these events remains unknown we have done a lot of advances
494 in this topic. We know that the SKIROC2 and 2a preamplifiers are referenced to the analog power
495 supply level, therefore, any voltage dip can be seen as signal by the preamplifiers. The presence of
496 a high inrush of current due to many channels triggered at the same time can create these voltage
497 dips. In previous studies (*i.e.* reference [24]), the ratio of retriggers and plane events was reduced
498 by improving the power supply stabilization capacitances. It is important to remark that all layers
499 and all ASICs analog and digital levels are powered using the same power supply. Moreover, the
500 high voltage power supply for the polarization of the PIN diode it is also common for all layers.
501 Therefore any noise in these power supplies or any overload of an ASIC may lead participate in the
502 creation of fake signals in different ASICs and layers.

503 Studying the MIP calibration data of this beam test we have noticed that most of the retriggers
504 and plane events are originated in ASICs far from the beam spot. Even more, hot spots tend appear
505 near the channels 37 and the channels tagged as “underflowed” during the commissioning phase.
506 The amount these events have been estimated to be of 1 – 3% in the ASICs where high frequency
507 interactions are produced (*i.e.* using 3 GeV positrons ate 2-3 KHz) and at higher rates even larger
508 than 40% in other ASICs far from the beam spot. Moreover, it has been noticed a correlation
509 between the time that an ASIC was full and the time of the appearance of some retriggers in other
510 areas of the PCB. This correlation corresponds to ~ 8 BCIDs (1.6 μ s) which hints of a distortion on
511 the analogue power supply when the signal that informs the DIF that one ASIC memory has been
512 filled is transmitted from the ASICs to the DIF through the PCB.

513 All this information and dedicated studies in the laboratory will be used for the improvement
514 of the power delivery, the PCB design and for further SKIROC developments with the possible
515 approval the ILC in the scope.

516 **5 Summary and prospects**

517 The R&D program of the highly granular SiW-ECAL detector is in an exciting phase. After the
518 proof of principle of the imaging calorimetry concept using the physics prototype, the technological
519 prototype is being constructed and tested. In this document we describe the commissioning and
520 beam test performance of a prototype built in with the first fully assembled detector elements (still
521 only 7 over the total of ~10000 to be in the ILD).

522 A very comprehensive and detailed commissioning procedure has been established and opti-
523 mized allowing us to identify and isolate the different noise sources that could spoil the data taking.
524 The beam test has provided a lot of useful data, allowing first for the study of the performance
525 of the detector and secondly for its channel by channel calibration. A full analysis including the
526 comparison with simulations of the second part of the data taking program (the electromagnetic
527 showers) is to come. During both phases, the commissioning and the beam test, we have collected
528 a good amount of data and results that will serve as input for future improvements on the design of
529 the ASUs, the SKIROC and the upstream DAQ.

530 In parallel to the work described here, several R&D efforts are being carried. For example, we
531 know that the ILD ECAL will host long layers of up to \sim 2.5m. A long layer constitutes a techno-
532 logical challenge in both aspects, the mechanical (very thin and long structure with fragile sensors
533 in the bottom, complicated assembly procedure...) and the electrical (i.e. transmission of signals
534 and high currents). For example, interconnections between ASUs and between ASU and interface
535 card are one of the most involved parts of the assembly and require close collaboration between
536 mechanical and electronic engineers. Therefore, many efforts are focused in the construction and
537 test of such long layers made of chains of ASUs (up to \sim 15 ASU) as well as in the standardization
538 of the interconnections. In addition, many efforts in the compactification of the DAQ and the ASUs
539 (i.e. the chip on board versions of the ASUs described in Section 2.3) are being conducted by the
540 SiW-ECAL collaboration.

541 Acknowledgments

542 This project has received funding from the European Union's Horizon 2020 Research and Innovation
543 program under Grant Agreement no. 654168. This work was supported by the P2IO LabEx (ANR-
544 10-LABX-0038), excellence project HIGHTEC, in the framework 'Investissements d'Avenir' (ANR-
545 11-IDEX-0003-01) managed by the French National Research Agency (ANR). The research leading
546 to these results has received funding from the People Programme (Marie Curie Actions) of the
547 European Union's Seventh Framework Programme (FP7/2007-2013) under REA grant agreement,
548 PCOFUND-GA-2013-609102, through the PRESTIGE programme coordinated by Campus France.
549 The measurements leading to these results have been performed at the Test Beam Facility at DESY
550 Hamburg (Germany), a member of the Helmholtz Association (HGF).

551 References

- 552 [1] T. Behnke, J. E. Brau, B. Foster, J. Fuster, M. Harrison, J. M. Paterson et al., *The International Linear
553 Collider Technical Design Report - Volume 1: Executive Summary*, [1306.6327](#).
- 554 [2] H. Baer, T. Barklow, K. Fujii, Y. Gao, A. Hoang, S. Kanemura et al., *The International Linear
555 Collider Technical Design Report - Volume 2: Physics*, [1306.6352](#).
- 556 [3] C. Adolphsen, M. Barone, B. Barish, K. Buesser, P. Burrows, J. Carwardine et al., *The International
557 Linear Collider Technical Design Report - Volume 3.I: Accelerator & in the Technical Design Phase*,
558 [1306.6353](#).
- 559 [4] C. Adolphsen, M. Barone, B. Barish, K. Buesser, P. Burrows, J. Carwardine et al., *The International
560 Linear Collider Technical Design Report - Volume 3.II: Accelerator Baseline Design*, [1306.6328](#).

- 561 [5] H. Abramowicz et al., *The International Linear Collider Technical Design Report - Volume 4:*
 562 *Detectors*, [1306.6329](#).
- 563 [6] M. Aicheler, P. Burrows, M. Draper, T. Garvey, P. Lebrun, K. Peach et al., *A Multi-TeV Linear*
 564 *Collider Based on CLIC Technology*, .
- 565 [7] L. Linssen, A. Miyamoto, M. Stanitzki and H. Weerts, *Physics and Detectors at CLIC: CLIC*
 566 *Conceptual Design Report*, [1202.5940](#).
- 567 [8] P. Lebrun, L. Linssen, A. Lucaci-Timoce, D. Schulte, F. Simon, S. Stapnes et al., *The CLIC*
 568 *Programme: Towards a Staged e+e- Linear Collider Exploring the Terascale : CLIC Conceptual*
 569 *Design Report*, [1209.2543](#).
- 570 [9] J.-C. Brient and H. Videau, *The Calorimetry at the future e+ e- linear collider*, *eConf* **C010630**
 571 (2001) E3047, [[hep-ex/0202004](#)].
- 572 [10] V. Morgunov and A. Raspereza, *Novel 3-D clustering algorithm and two particle separation with tile*
 573 *HCAL*, in *Linear colliders. Proceedings, International Conference, LCWS 2004, Paris, France, April*
 574 *19-23, 2004*, pp. 431–436, 2004. [physics/0412108](#).
- 575 [11] F. Sefkow, A. White, K. Kawagoe, R. Pöschl and J. Repond, *Experimental Tests of Particle Flow*
 576 *Calorimetry*, *Rev. Mod. Phys.* **88** (2016) 015003, [[1507.05893](#)].
- 577 [12] CALICE collaboration, C. Adloff, J. Blaha, J. J. Blaising, C. Drancourt, A. Espargiliere, R. Galione
 578 et al., *Tests of a particle flow algorithm with CALICE test beam data*, *JINST* **6** (2011) P07005,
 579 [[1105.3417](#)].
- 580 [13] CALICE collaboration, J. Repond et al., *Design and Electronics Commissioning of the Physics*
 581 *Prototype of a Si-W Electromagnetic Calorimeter for the International Linear Collider*, *JINST* **3**
 582 (2008) P08001, [[0805.4833](#)].
- 583 [14] CALICE collaboration, C. Adloff et al., *Response of the CALICE Si-W electromagnetic calorimeter*
 584 *physics prototype to electrons*, *Nucl. Instrum. Meth.* **A608** (2009) 372–383, [[0811.2354](#)].
- 585 [15] C. Adloff et al., *Study of the interactions of pions in the CALICE silicon-tungsten calorimeter*
 586 *prototype*, *JINST* **5** (2010) P05007, [[1004.4996](#)].
- 587 [16] CALICE collaboration, C. Adloff et al., *Effects of high-energy particle showers on the embedded*
 588 *front-end electronics of an electromagnetic calorimeter for a future lepton collider*, *Nucl. Instrum.*
 589 *Meth.* **A654** (2011) 97–109, [[1102.3454](#)].
- 590 [17] CALICE collaboration, B. Bilki et al., *Testing hadronic interaction models using a highly granular*
 591 *silicon-tungsten calorimeter*, *Nucl. Instrum. Meth.* **A794** (2015) 240–254, [[1411.7215](#)].
- 592 [18] CALICE collaboration, R. Cornat and R. Pöeschl, *Technological prototype of a silicon-tungsten*
 593 *imaging electromagnetic calorimeter*, *JINST* **10** (2015) C06015.
- 594 [19] CALICE collaboration, R. Cornat, *Semiconductor sensors for the CALICE SiW EMC and study of the*
 595 *cross-talk between guard rings and pixels in the CALICE SiW prototype*, *J. Phys. Conf. Ser.* **160**
 596 (2009) 012067.
- 597 [20] S. Callier, F. Dulucq, C. de La Taille, G. Martin-Chassard and N. Seguin-Moreau, *SKIROC2, front*
 598 *end chip designed to readout the Electromagnetic CALorimeter at the ILC*, *JINST* **6** (2011) C12040.
- 599 [21] F. Gastaldi, R. Cornat, F. Magniette and V. Boudry, *A scalable gigabit data acquisition system for*
 600 *calorimeters for linear collider*, *PoS TIPP2014* (2014) 193.
- 601 [22] M. Rubio-Roy, F. Thiant and F. Magniette, *Flexible online monitoring for high-energy physics with*
 602 *Pyrame*, *J. Phys. Conf. Ser.* **898** (2017) 032009.

- 603 [23] CALICE collaboration, F. Magniette and A. Irles, *Pyrame 3, an online framework for Calice*
604 *SiW-Ecal*, *JINST* **13** (2018) C03009.
- 605 [24] M. S. Amjad et al., *Beam test performance of the SKIROC2 ASIC*, *Nucl. Instrum. Meth. A* **778** (2015)
606 78–84.
- 607 [25] T. Suehara et al., *Performance study of SKIROC2/A ASIC for ILD Si-W ECAL*, *JINST* **13** (2018)
608 C03015, [[1801.02024](#)].